JOUL, Volume *2*

Supplemental Information

Trapping an Iron(VI) Water-Splitting Intermediate in Nonaqueous Media

Bryan M. Hunter, Niklas B. Thompson, Astrid M. Müller, George R. Rossman, Michael G. Hill, Jay R. Winkler, and Harry B. Gray

S1: Tafel Behavior

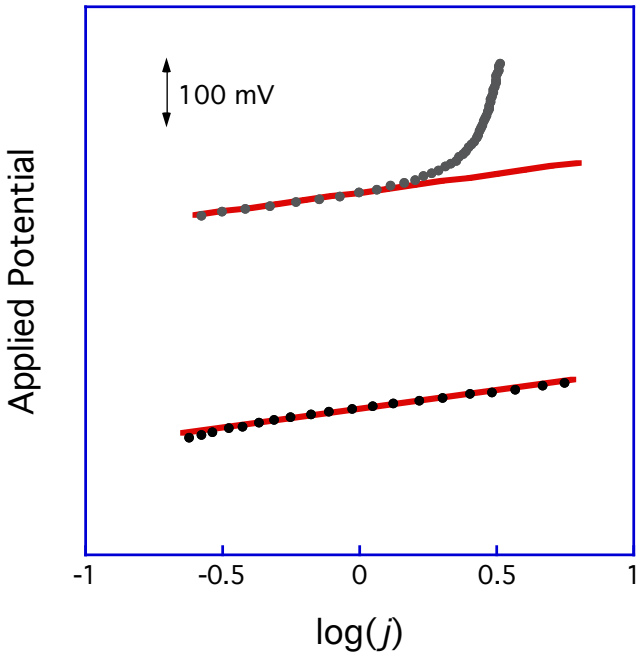

Figure S1: Tafel plot of [NiFe]-LDH on a rotated disk (900 RPM). (Top) 1% 1 *M* aqueous KOH in acetonitrile; (bottom) 1 *M* aqueous KOH. The y-axis represents arbitrary potential, since the overpotential in acetonitrile is undefined. The x-axis is the logarithm of the current density. The 1% 1 *M* aqueous KOH in acetonitrile plot curves upward at high applied potential due to mass transport limitation at low substrate concentration. The units for *j* are mA/cm^2.

Table S1: Least-squares fitting parameters for Tafel behavior of [NiFe]-LDH in 1 *M* aqueous KOH.

Y = M0 + M1*X						
	Value	Std. Error	t Value	P Value	Lower 95%	Upper 95%
M0	476.52	0.29161	1634.1	5.9385e-195	475.95	477.1
M1	59.149	0.68233	86.686	1.7499e-85	57.792	60.505
Goodness of Fit						
R	0.99433					
Adj. R^2	0.98855					
Std. Error	2.7333					
F Value	7514.5					
P Value	1.7499e-85					

S2: Kinetics Simulations

We have simulated the kinetics of a compressed version of the mechanism illustrated in Fig. 5. We assume that two electrons and two protons are removed from the catalyst in the first step to produce the highly oxidized intermediate; two hydroxide ions react with the oxidized catalyst in the second step to generate oxygen. When ample hydroxide ion is present as in 1 *M* KOH, the population of the intermediate is very low and would be difficult to detect in *operando* measurements. When H_2O and HO^- concentrations are restricted as in acetonitrile solvent, oxygen production is inhibited and the population of the oxidized catalyst intermediate increases substantially to the point that it would be spectroscopically detectable. The simulation results closely mirror our experimental observations.

A compressed version of the mechanism outline in Figure 5 is given by the following reaction steps, where CAT is the resting form of the electrocatalyst and CAT_{ox} is the oxidized form in which 2 electrons, 2 protons, and 1 water molecule have been removed. The two reaction steps defined by rate constants k_{1a} and k_{1b} differ only in the identity of the proton acceptor (HO^- or H_2O).

$$2HO^- + CAT \xrightarrow{k_{1a}} 3H_2O + CAT_{ox} + 4e^-$$

$$H_2O + CAT \xrightarrow{k_{1b}} 2H_3O^+ + CAT_{ox} + 4e^-$$

$$H_2O + CAT_{ox} + 2HO^- \xrightarrow{k_2} O_2 + CAT$$

$$2H_2O \underset{k_{-3}}{\overset{k_3}{\longleftrightarrow}} H_3O^+ + HO^- \qquad K_{eq} = \frac{K_w}{[H_2O]^2} = \frac{k_3}{k_{-3}} = 3.25 \times 10^{-18}$$

Under the assumption of instantaneous mixing of electrode products with the bulk solution, the conversion rates of all reagents are given by following differential equations:

$$\frac{d[CAT]}{dt}\left(\frac{mol}{cm^2 s}\right) = -k_{1a}[CAT][HO^-]^2 - k_{1b}[CAT][H_2O] + k_2[CAT_{ox}][HO^-]^2[H_2O]$$

$$\frac{d[CAT_{ox}]}{dt}\left(\frac{mol}{cm^2 s}\right) = k_{1a}[CAT][HO^-]^2 + k_{1b}[CAT][H_2O] - k_2[CAT_{ox}][HO^-]^2[H_2O]$$

$$\frac{d[HO^-]}{dt}\left(\frac{mol}{L\, s}\right) = -2\times10^{-3}k_{1a}[CAT][HO^-]^2 - 2\times10^{-3}k_2[CAT_{ox}][HO^-]^2[H_2O] + k_3[H_2O]^2 - k_{-3}[H_3O^+][HO^-]$$

$$\frac{d[H_2O]}{dt}\left(\frac{mol}{L\, s}\right) = 3\times10^{-3}k_{1a}[CAT][HO^-]^2 - 1\times10^{-3}k_{1b}[CAT][H_2O] - 1\times10^{-3}k_2[CAT_{ox}][HO^-]^2[H_2O] - 2k_3[H_2O]^2 + 2k_{-3}[H_3O^+][HO^-]$$

$$\frac{d[H_3O^+]}{dt}\left(\frac{mol}{L\, s}\right) = 2\times10^{-3}k_{1b}[CAT][H_2O] + k_3[H_2O]^2 - k_{-3}[H_3O^+][HO^-]$$

$$\frac{d[O_2]}{dt}\left(\frac{mol}{L\, s}\right) = 1\times10^{-3}k_2[CAT_{ox}][HO^-]^2[H_2O]$$

The differential equations were solved numerically using the MATLAB function *ide23s* (for stiff equations, Set 1), and *ide23* (Set 2). The accuracy of the numerical solutions was

tested by numerically differentiating the six time-dependent concentration profiles for each reagent and comparing those to the combinations of rate constants and concentrations defined by the differential equations.

Using an estimated catalyst surface area of 193 m^2g^{-1} and assuming a 20% population of Fe centers, the initial catalysts concentration was taken to be $[CAT]_0 = 10^{-9}$ mol cm^{-2}. The initial concentrations of oxidized catalyst, $[CAT_{ox}]_0$, and oxygen, $[O_2]$, were set equal to zero. Two sets of initial substrate concentration conditions were considered. Set 1 corresponds to aqueous conditions: $[H_2O]_0 = 55.5$ M; $[HO^-]_0 = 1$ M; $[H_3O^+]_0 = 10^{-14}$ M. Set 2 corresponds to nonaqueous electrolyte conditions: $[H_2O]_0 = 5 \times 10^{-3}$ M; $[HO^-]_0 = 9 \times 10^{-12}$ M; $[H_3O^+]_0 = 9 \times 10^{-12}$ M.

The rate constants were given the following values:

$k_{1a} = 3 \times 10^6$ $M^{-2}s^{-1}$; defined to produce O_2 at a rate of 2.6×10^{-6} M s^{-1}

$k_{1b} = 1 \times 10^2$ $M^{-1}s^{-1}$; defined to not contribute to O_2 production under aqueous pH 14 conditions (set 1)

$k_2 = 1 \times 10^8$ $M^{-3}s^{-1}$; defined to be large enough relative to k_{1a} so that the steady state ratio of $[CAT_{ox}]$:[CAT] is less than 10^{-3} under aqueous pH 14 conditions (set 1)

$k_3 = 1 \times 10^{10}$ $M^{-1}s^{-1}$; assumed to be diffusion controlled

$k_{-3} = 3.25 \times 10^{-8}$ $M^{-1}s^{-1}$; defined by k_3 and K_{eq}

With these parameter sets, the simulations produce the time-dependent concentration profiles and $[CAT_{ox}]$:[CAT] ratios shown in Figure S2 (set 1 conditions) and Figure S3 (set 2 conditions). Under aqueous pH 14 conditions (set 1), O_2 is produced at the specified rate and the $[CAT_{ox}]$:[CAT] ratio remains less than 10^{-3}. Under nonaqueous conditions (set 2), the concentration of CAT_{ox} builds up over time and the $[CAT_{ox}]$:[CAT] ratio becomes greater than 1 after 1 s.

The simulations are not intended to accurately reproduce the experimental electrochemical kinetics. Rather, they are meant to show that the mechanism in Figure 5 is plausible and can lead to the general behavior found experimentally. In particular, the simulations demonstrate that while no oxidized intermediate would be detected during turnover conditions in aqueous alkaline solution, the intermediate would be expected to build up when a nonaqueous electrolyte is employed.

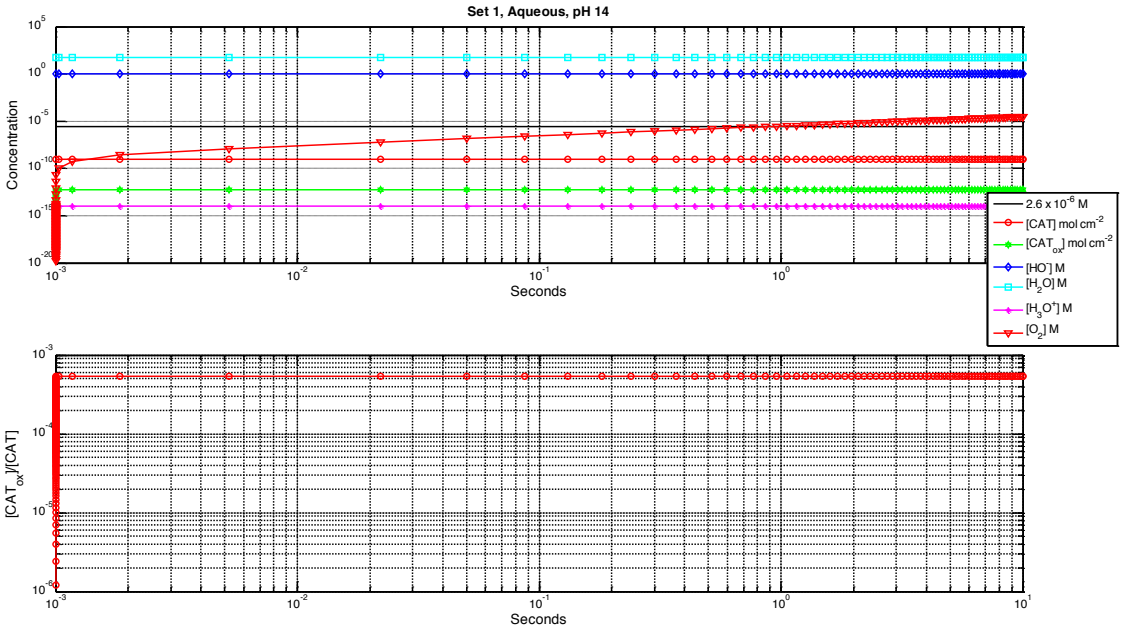

Figure S2. Simulated concentration versus time profiles generated by numerical integration of differential equations listed in the supporting text. Initial conditions were aqueous pH 14 electrolyte (Set 1).

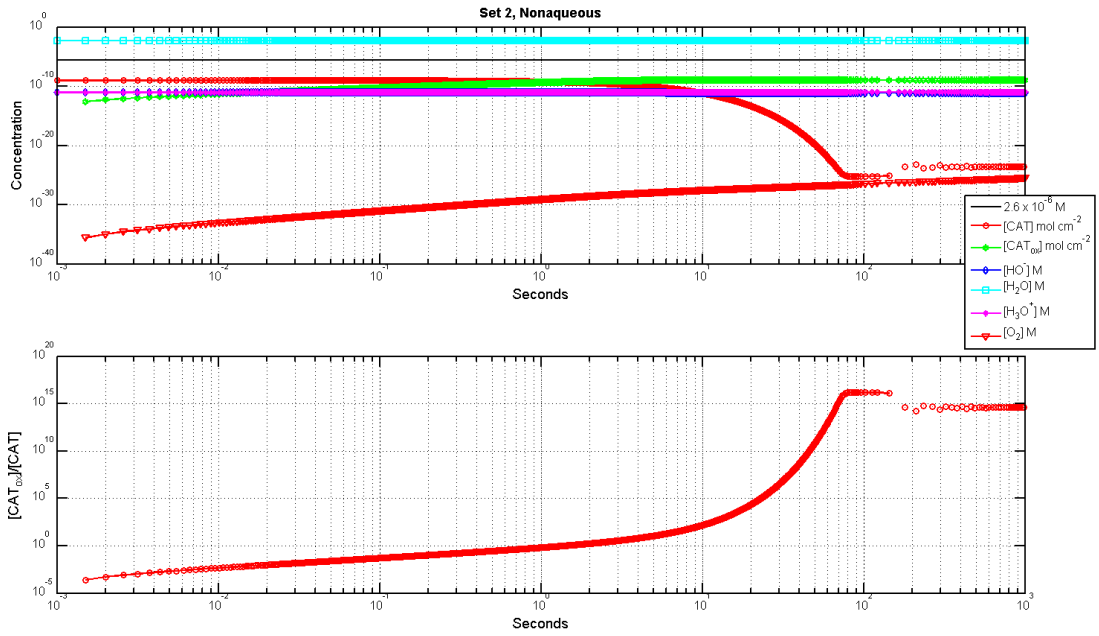

Figure S3. Simulated concentration versus time profiles generated by numerical integration of differential equations listed in the supporting text. Initial conditions were nonaqueous electrolyte (Set 2).

S3: Estimation of the Standard Electrode Potential for the Fe(IV)/Fe(III) Couple in "Dry" Acetonitrile

$$Fe^{IV}(O)_{(s)} + H^{+}_{(aq)}\ e^{-} \rightleftharpoons Fe^{III}(OH)_{(s)} \qquad \textbf{(Equation S1.)}$$

The standard electrode potential for Equation S1 in terms of the free energies of formation of $Fe^{IV}(O)_{(s)}$ (x)and $Fe^{III}(OH)_{(s)}$ (y) can be estimated from thermodynamic cycles as shown in Schemes S1 and S2. Here, "dry" is taken to mean the condition where [H_2O] approaches the limit of a dilute acetonitrile solution of H_2O, as per Matsubara (ref. 17). All values taken from reference 17 unless otherwise stated.

Scheme S1. A thermodynamic cycle to estimate the potential for equation S1 at standard conditions (1 *M* $H^{+}_{(aq)}$) and 298 K.

$Fe^{IV}(O)_{(s)} + H^{+}_{(aq)}\ e^{-} \rightleftharpoons Fe^{III}(OH)_{(s)}$	$\Delta_r G_{aq}°$	kJ/mol
$Fe^{IV}(O)_{(s)} \rightleftharpoons Fe_{(s)} + 1/2O_{2(g)}$	$-\Delta_f G_{FeO}°$	$-x$
$Fe_{(s)} + 1/2O_{2(g)} + 1/2H_{2(g)} \rightleftharpoons Fe^{III}(OH)_{(s)}$	$\Delta_f G_{FeOH}°$	y
$H^{+}_{(aq)} \rightleftharpoons H^{+}_{(sol)}$	$\Delta_{tr}{}^{aq\rightarrow CH3CN}G_1°$	46.2
$H^{+}_{(sol)} + e^{-} \rightleftharpoons 1/2H_{2(g)}$	$\Delta_r G_1°$	2.5 (*vs* Fc^{+}/Fc)

Scheme S2. A thermodynamic cycle to estimate the potential for equation S1 in "dry" acetonitrile at 298 K. As in reference C, the subscripts "(g)", "(aq)", "(sol)", and "(sol, x)" denote substances in gas, aqueous solution, acetonitrile solution, and acetonitrile solution phases, whose activities are expressed in units of pressure (bar), molarity (M), molarity (M), and mole fraction (x), respectively. Matsubara notes that "$H_2O_{(sol,\ x\rightarrow 0)}$ denotes H_2O at the limit of a dilute acetonitrile solution of H_2O where the standard state for H_2O is taken to be unit mole fraction of H_2O (i.e., pure liquid water)."

$Fe^{IV}(O)_{(s)} + H^{+}_{(aq)}\ e^{-} \rightleftharpoons Fe^{III}(OH)_{(s)}$	$\Delta_r G_{acn}°$	kJ/mol
$3H^{+}_{(sol)} + 3e^{-} \rightleftharpoons 3/2H_{2(g)}$	$\Delta_r G_1°$	2.5(3) (Fc^{+}/Fc)
$H_{2(g)} + 1/2O_{2(g)} \rightleftharpoons H_2O_{(g)}$	$\Delta_r G_2°$	-228.582
$H_2O_{(g)} \rightleftharpoons H_2O_{(sol,x\rightarrow 0)}$	$\Delta_{tr}{}^{g\rightarrow CH3CN}G_2°$	-3.2
$2H_2O_{(sol,x\rightarrow 0)} \rightleftharpoons 2H^{+}_{(sol)} + 2OH^{-}_{(sol)}$	$\Delta G_w°$	79.9(2)
$2OH^{-}_{(sol)} \rightleftharpoons 1/2O_{2(g)} + H_2O_{(sol,x\rightarrow 0)} + 2e^{-}$	$\Delta_r G_{ox}°$	199[a]
$Fe^{IV}(O)_{(s)} \rightleftharpoons Fe_{(s)} + 1/2O_{2(g)}$	$-\Delta_f G_{FeO}°$	$-x$
$Fe_{(s)} + 1/2O_{2(g)} + 1/2H_{2(g)} \rightleftharpoons Fe^{III}(OH)_{(s)}$	$\Delta_f G_{FeOH}°$	y

[a] Calculated from $E°$ = -0.401 *vs* NHE [Dean, J. A., & Lange, N. A. (1999). *Lange's handbook of chemistry*. New York: McGraw-Hill.] referenced to Fc^{+}/Fc [Pavlishchuk, V. V., Addison, A. W. Conversion constants for redox potentials measured versus different reference electrodes in acetonitrile solutions at 25°C. *Inorg. Chim. Acta* **1**, 97-102 (2000)] and converted to free energy by $\Delta G° = -nFE°$ for n = 2.

Following Schemes S1 and S2, the standard electrode potentials for Equation S1 are:

$$\Delta_r G_{aq}^\circ = \frac{-(-\Delta_f G_{FeO}^\circ + \Delta_f G_{FeOH}^\circ + \Delta_{tr}{}^{aq\rightarrow CH3CN} G_1^\circ + \Delta_r G_1^\circ)}{F} = A - 0.505\ V,$$

where $A = \frac{x-y}{F}$.

$$\Delta_r G_{acn}^\circ = \frac{-(3\Delta_r G_1^\circ + \Delta_r G_2^\circ + \Delta_{tr}{}^{g\rightarrow CH3CN} G_2^\circ + 2\Delta G_w^\circ + \Delta_r G_{ox}^\circ - \Delta_f G_{FeO}^\circ + \Delta_f G_{FeOH}^\circ)}{F}$$

$$= A + 1.39\ V.$$

Thus, the potential of the Fe(IV)/Fe(III) couple is shifted positive by over 1.5V in the theoretical limit of "dry" acetonitrile.

S4: Supporting Electrochemistry

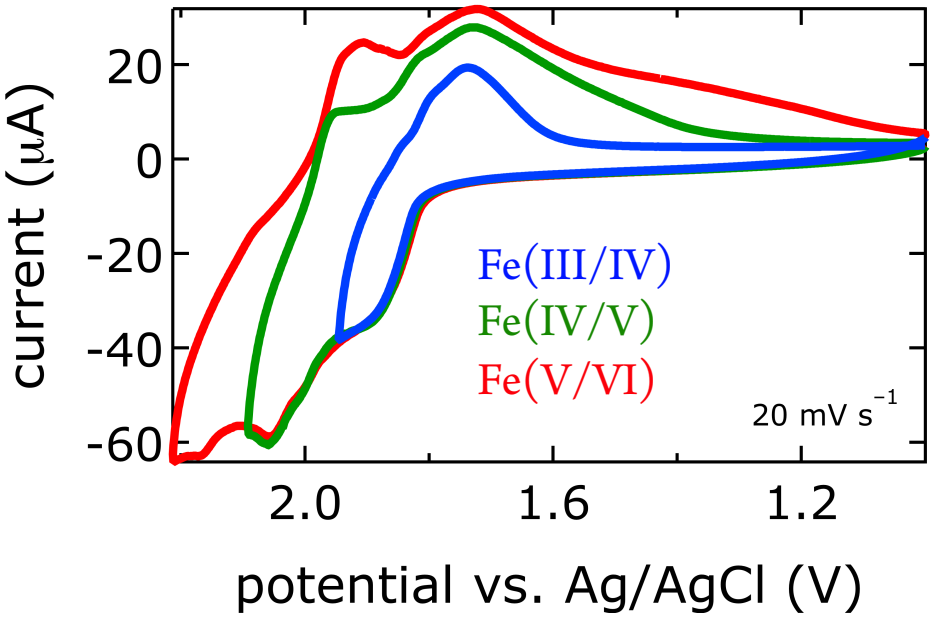

Figure S4: Cyclic voltammetry of [NiFe]-LDH in 0.1 *M* tetrabutylammonium hexafluorophosphate ([TBA]PF_6) in acetonitrile. The scans were reversed after each oxidative event, showing that each was coupled to a corresponding reduction. Scan rate was 20 mV s^{-1}.

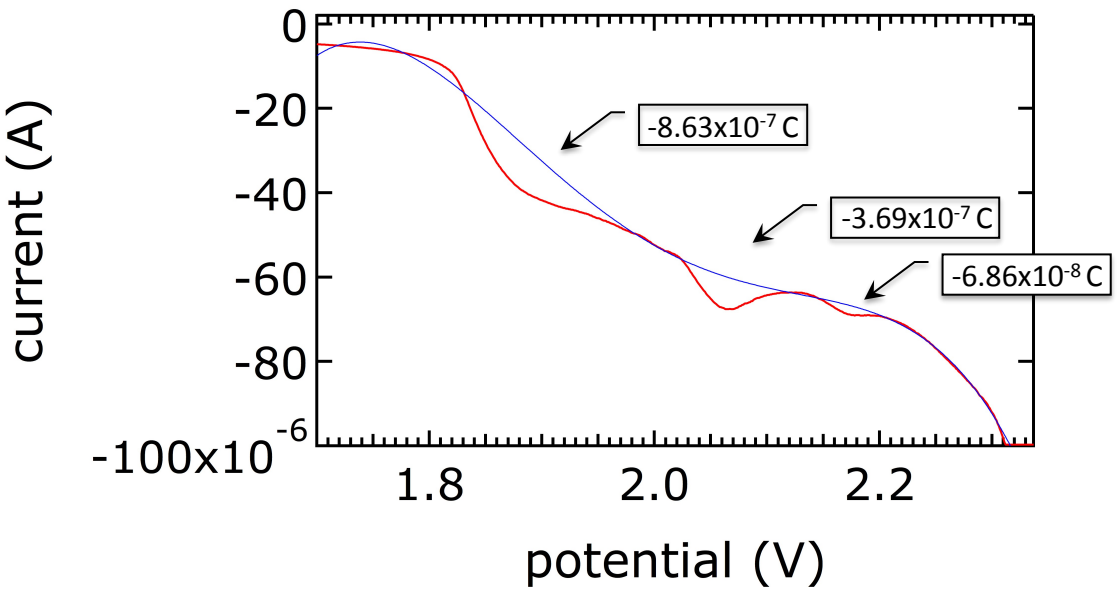

Figure S5: Cyclic voltammetry of [NiFe]-LDH in 0.1 *M* tetrabutylammonium hexafluorophosphate ([TBA]PF_6) in acetonitrile with cubic spline baseline subtraction (blue) and charge passed integrated for the 3 iron-based features. Reference electrode: Ag/AgCl.

Table S2: Calculation of activity of iron in [NiFe]-LDH sample, based on coulometry of cyclic voltammetry. These calculations assume a formula of $Ni_{0.78}Fe_{0.22}(OH)_2(NO_3)_{0.22}$, and a catalyst loading of 20 μL of a 2 mg/mL solution.

	Charge Passed	Active Moles	% active
1st oxidation	-8.63×10^{-7}	8.94×10^{-12}	0.00237
2nd oxidation	-3.69×10^{-7}	3.82×10^{-12}	0.00101
3rd oxidation	-6.86×10^{-8}	7.11×10^{-13}	0.000188

S5: Supporting Spectroelectrochemistry

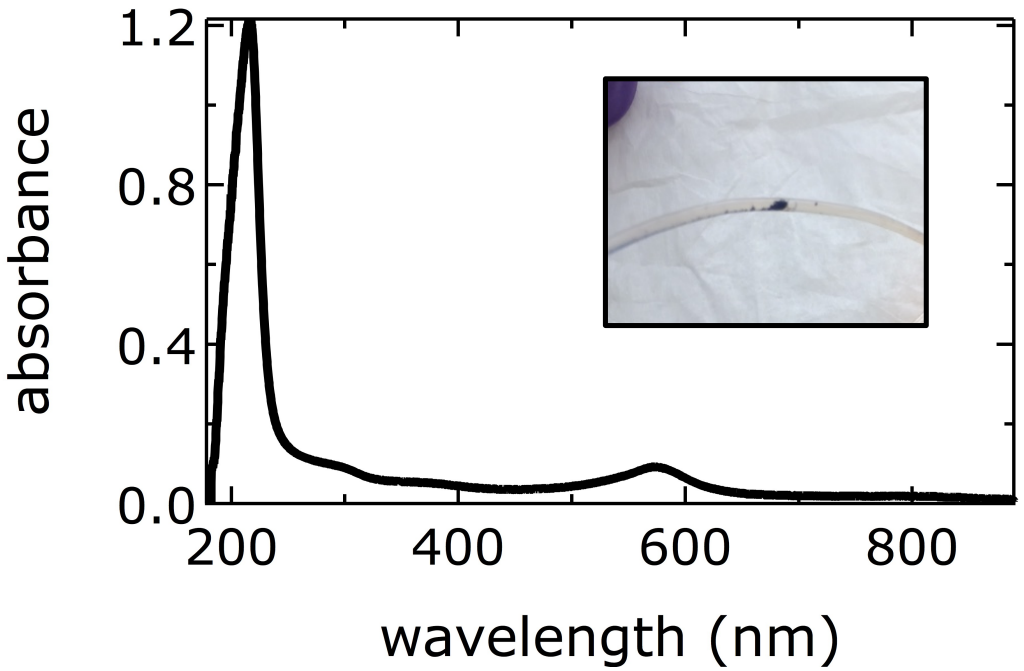

Figure S6: UV-visible spectrum of small volume electrolysis electrolyte following 10 minutes of anodic polarization; (Inset) typical purple substance that leaches out during spectroelectrochemistry experiments.

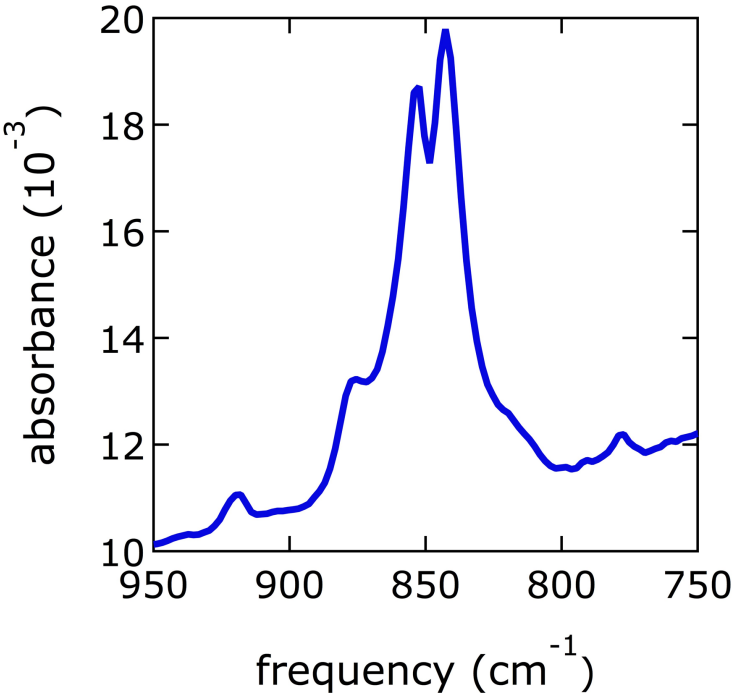

Figure S7: Infrared spectroelectrochemistry experiment performed without Nafion®. Three-pronged signal upon bulk oxidation in acetonitrile (2.3 V *vs.* Pt), 0.1 M [TBA]PF_6, on GC working electrode, Pt counter electrode.

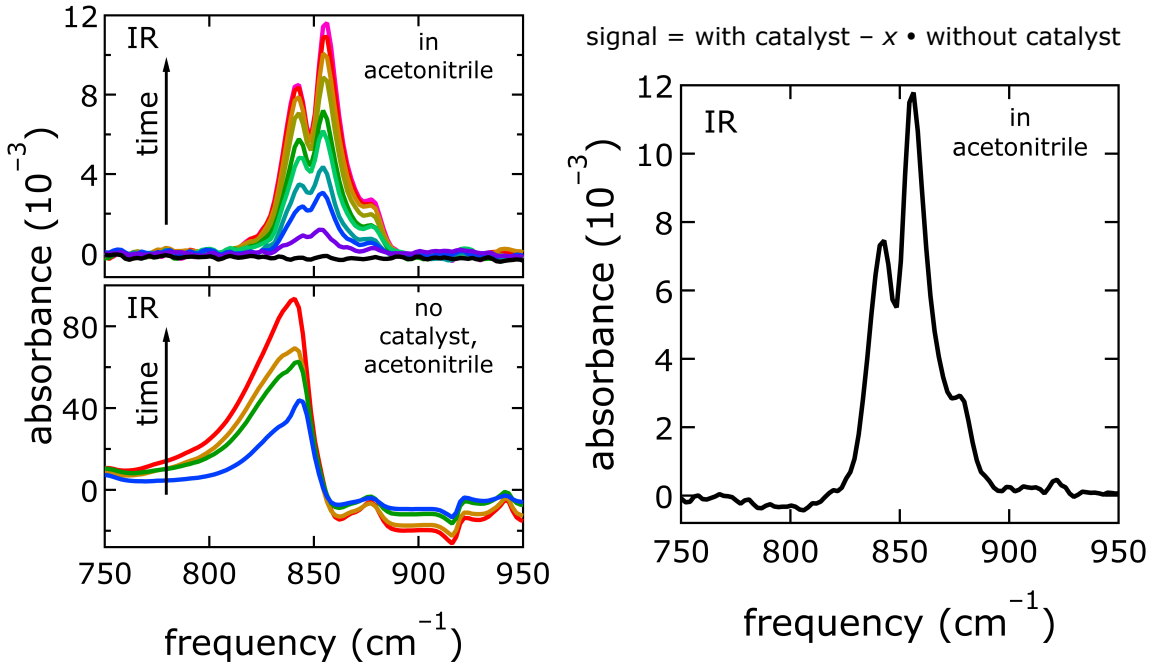

Figure S8: (top left) Three-pronged signal growing in upon bulk oxidation in acetonitrile (2.3 V *vs.* Pt), 0.1 M [TBA]PF_6, on GC working electrode, Pt counter electrode, 30 s between spectra; (bottom left) bare electrode signal when polarized at 2.3 V *vs.* Pt in acetonitrile, 30 s between spectra; (right) bare electrode signal subtracted from catalyst signal, showing that three-pronged signal remains after background subtraction.

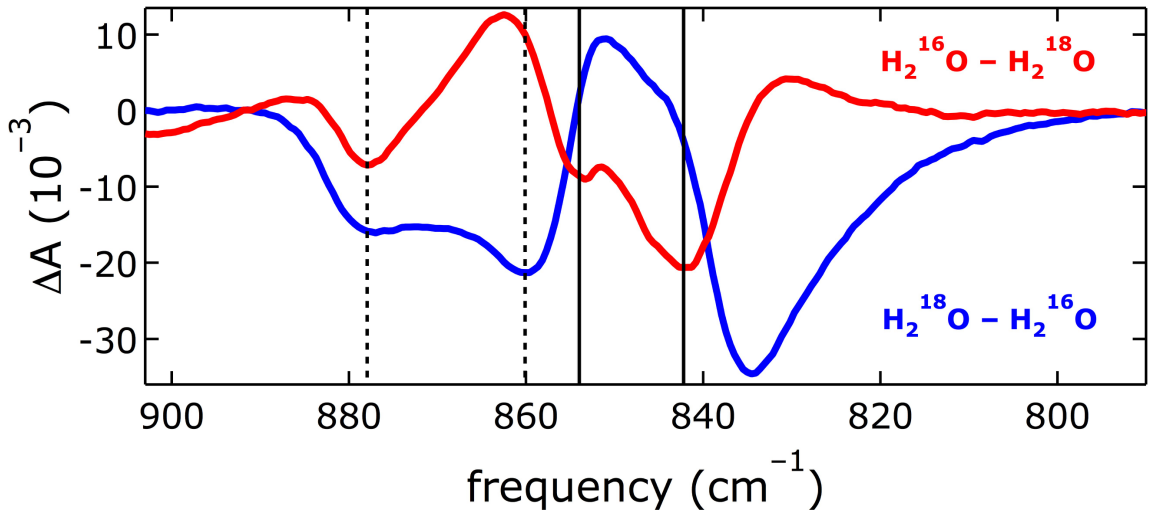

Figure S9: Partial isotope exchange experiment. Electrode was polarized at 2.3 V *vs.* Pt in acetonitrile, background taken, and quenched with 5% $H_2{}^{18}O$ in acetonitrile. Re-polarization at 2.3 V produced the blue trace ($H_2{}^{18}O$ – $H_2{}^{16}O$). A second background was taken and the electrode was quenched with 5% $H_2{}^{16}O$ in acetonitrile. Re-polarization at 2.3 V produced the red trace ($H_2{}^{16}O$ – $H_2{}^{18}O$).

S5: Stability of Acetonitrile under Anodic Polarization

Since the infrared spectroelectrochemical experiments were performed close to the anodic limit of acetonitrile, they were repeated in nitromethane. The spectra obtained were virtually identical (Figure S10).

At high potentials (*ca.* 2.2 V *vs.* SCE), the formation of CO_2 and acetamide have been observed in $LiClO_4/CH_3CN$ electrolytes on Pt and glassy carbon electrodes (P. Krtil, L. Kavan, and P. Novák, Oxidation of acetonitrile-based electrolyte solutions at high potentials. An in situ Fourier transform infrared spectroscopy study, *J. Electrochem. Soc.* **140,** 1993, 3390-3395).

Additionally, an uncharacterized "nitrogen oxide" has been detected by infrared spectroscopy at platinum electrodes. This decomposition is activated by trace water and platinum anodes.

We detected none of these decomposition products by infrared spectroscopy, and our water concentration was *ca*. ten times lower than that employed in Krtil et al. (0.003-0.05 M).

Furthermore, the ^{18}O isotopic shifts of the observed species are inconsistent with the known decomposition products of acetonitrile.

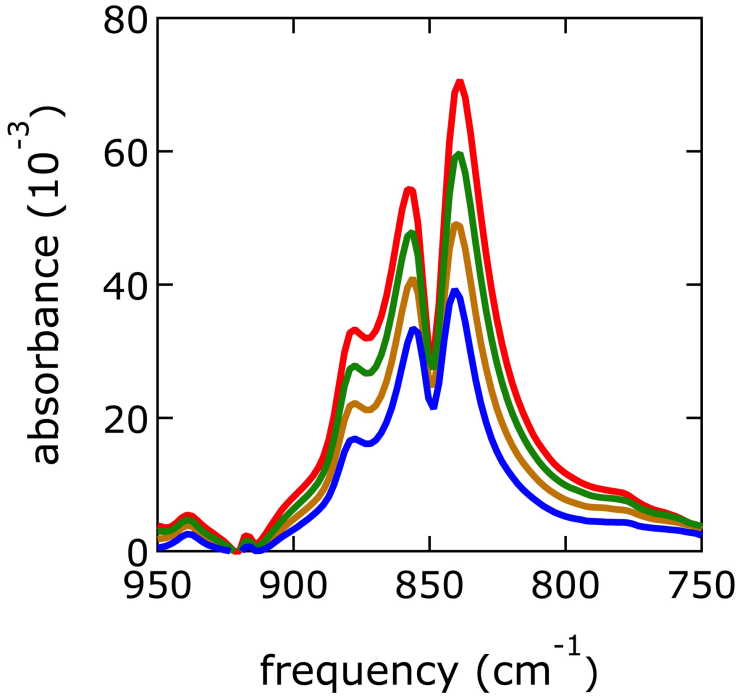

Figure S10: Infrared spectroelectrochemistry experiment performed in nitromethane. Three-pronged signal growing in upon bulk oxidation in nitromethane (2.3 V *vs.* Pt), 0.1 M [TBA]PF_6, on GC working electrode, Pt counter electrode, 30 s between spectra.

S6: Supporting Raman Spectroscopy

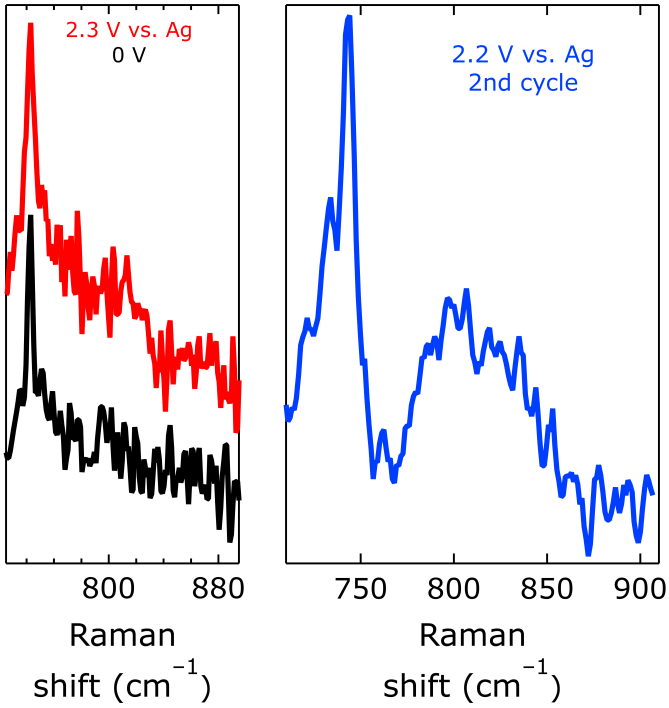

Figure S11: Raman spectroelectrochemistry experiment in acetonitrile. Weak signal observed at ~800 cm^{-1} upon polarization of the electrode at 2.3 V (left) and 2.2 V (right) *vs.* Pt in acetonitrile, 0.1 M [TBA]PF_6, on GC working electrode, and Pt counter electrode. The signal is larger on the second polarization cycle (right). The excitation wavelength was 514.3 nm.

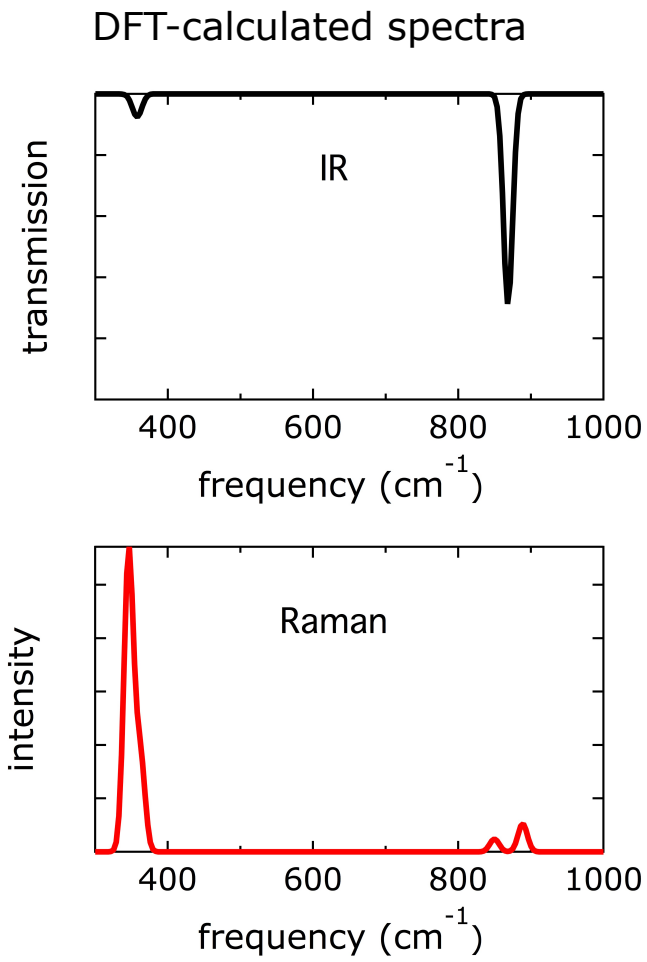

Figure S12: (Top) Calculated infrared spectrum for ferrate; (bottom) calculated Raman spectrum for ferrate.

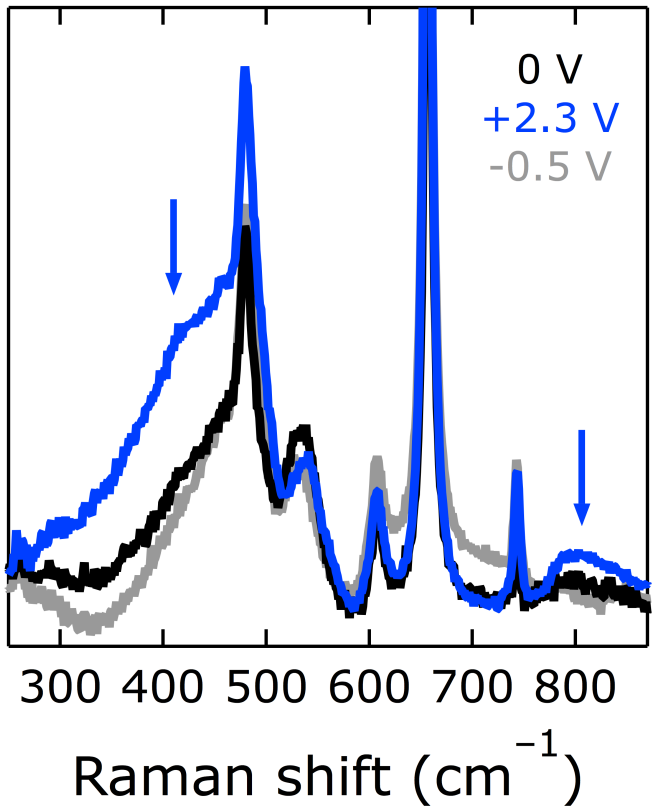

Figure S13: Raman spectroelectrochemistry experiment in nitromethane. Signal observed in the bending region (~400 cm^{-1}) upon polarization of the electrode at 2.3 V *vs.* Pt (blue). The signal is diminished upon cycling to -0.5 V *vs.* Pt (gray). Nitromethane, 0.1 M [TBA]PF_6, on GC working electrode, Pt counter electrode, and Pt reference electrode. The excitation wavelength was 514.3 nm.

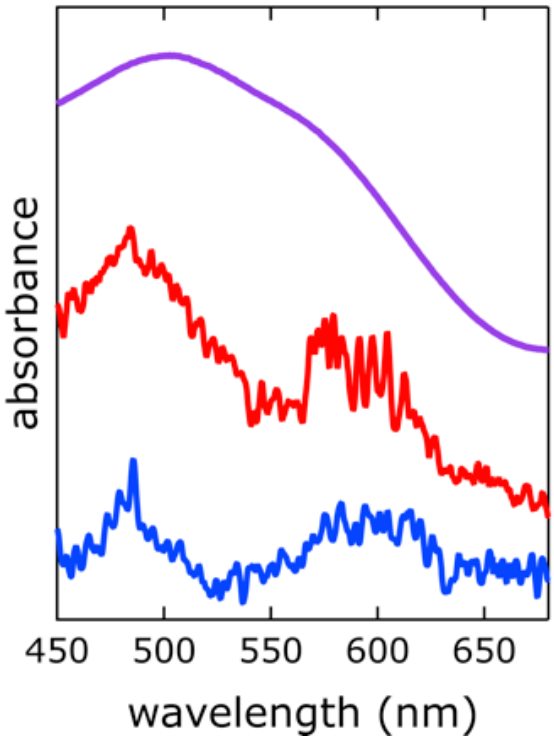

Figure S14: UV-visible spectra of [NiFe]-LDH after *in-situ* polarization at 2.3 V *vs.* Pt (blue) and chemical oxidation by 30% hydrogen peroxide (red). UV-visible spectrum of potassium ferrate (K_2FeO_4) in water at pH 7.0 (purple).

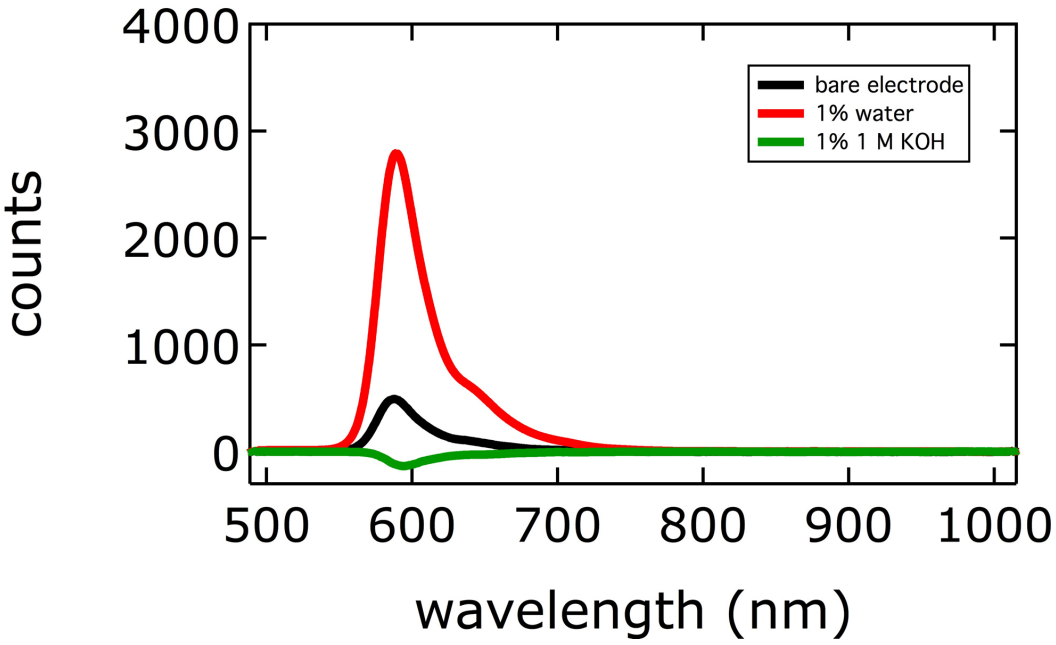

Figure S15: Steady-state fluorescence detection of hydrogen peroxide using Amplex® Red reagent. Fluorescence intensity is directly proportional to peroxide concentration. Fluorescence from the stock electrolyte solution has been subtracted, giving rise to a small "negative" region around 600 nm for the green trace.

S7: Oxygen Detection

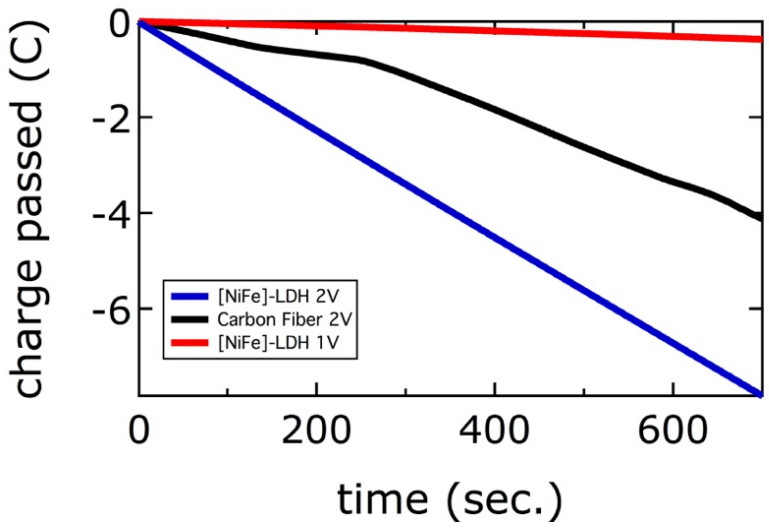

Figure S16: Chronocoulometric traces for $Ir(dppe)_2Cl$ oxygen trapping experiments.

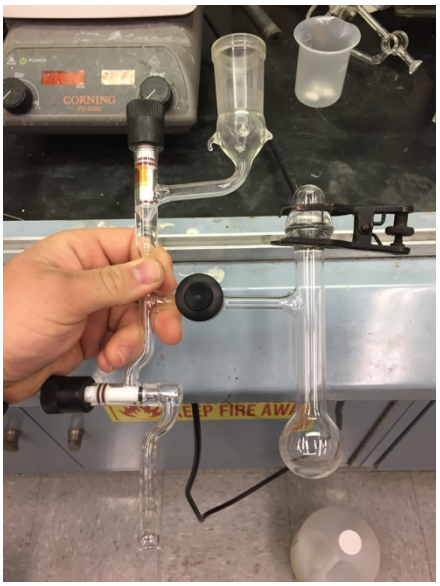

Figure S17: Custom laser cell for $Ir(dppe)_2Cl$ oxygen binding experiments. Design allows the introduction of macroscopic carbon fiber electrodes while maintaining an oxygen-free atmosphere.

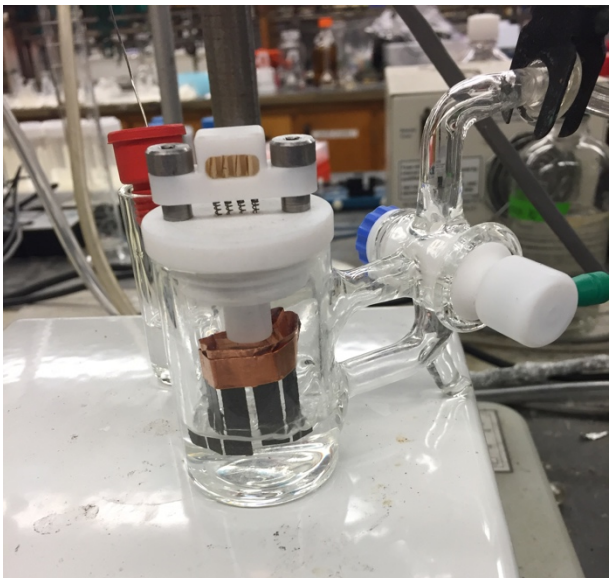

Figure S18: Electrochemical cell for $Ir(dppe)_2Cl$ oxygen binding experiments. Electrodes are individual carbon fiber strips, held by copper tape.

S8: Mössbauer Spectroscopy

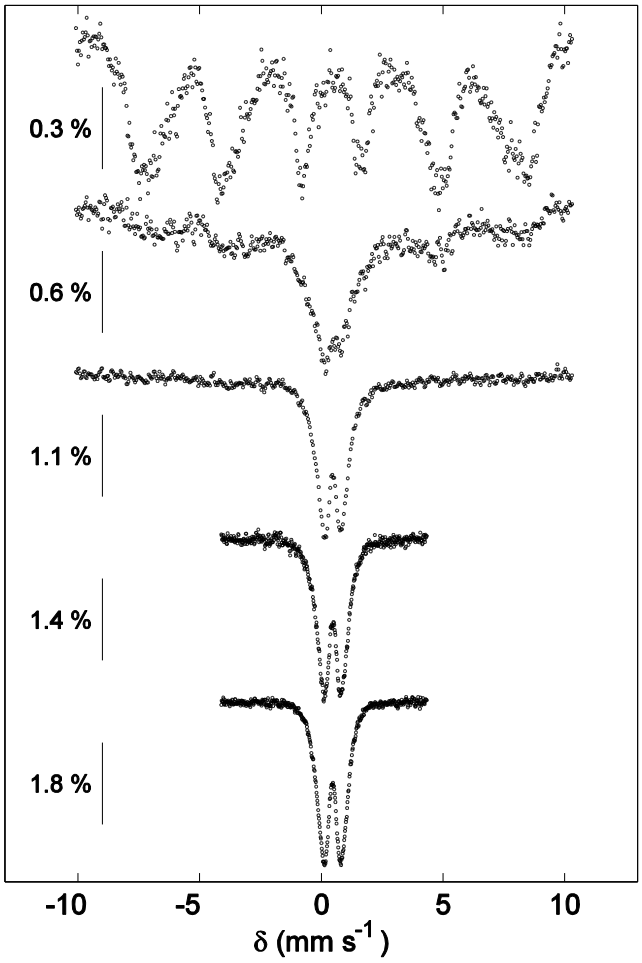

Figure S19: Temperature dependence of the Mössbauer signal of [Ni^{57}Fe]-LDH, polarized at 2 V *vs*. Pt, in zero applied field. From top to bottom, spectra were collected at 5, 15, 30, 50, and 80 K. The absorbance scale for each spectrum is indicated by the bar to the left.

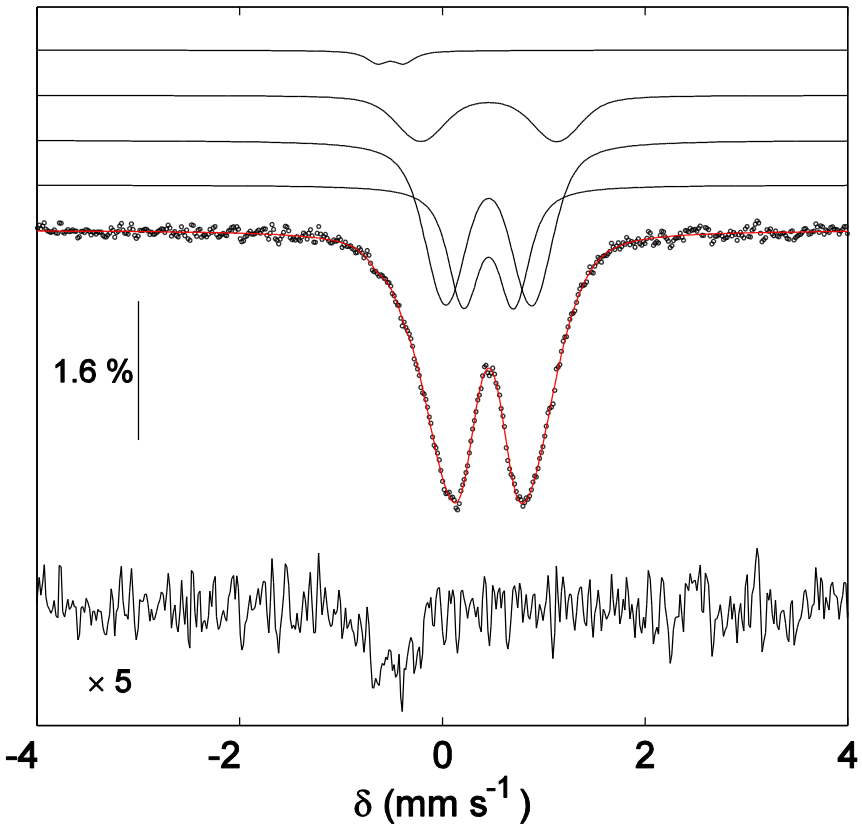

Figure S20: The zero field Mössbauer spectrum of [Ni^{57}Fe]-LDH, polarized at 2 V *vs.* Pt, collected at 100 K. The raw data are presented as open black circles, with the simulated spectrum shown in red. Individual sub-spectra are plotted as black lines above the raw data. Below is a subtraction of the simulated Fe(III) components from the data, showing the presence of a small amount of oxidized Fe present as a shoulder in the raw data.

Table S3: Simulation for [Ni^{57}Fe]-LDH polarized at 2 V *vs*. Pt, at 100 K using a hyperfine distribution model.

	Parameters			
	***N* = 1**	***N* = 2**	***N* = 3**	**Final fit**
$\Delta E_{Q,1}$ (mm s^{-1})	0.791	0.619	0.590	0.498
σ_1 (mm s^{-1})	0.578	0.520	0.549	0.366
p_1 (mm s^{-1})	1.078	0.546	0.603	0.305
$\Delta E_{Q,1}$ (mm s^{-1})		1.098	1.095	0.852
σ_1 (mm s^{-1})		0.956	0.576	0.648
p_1 (mm s^{-1})		0.487	0.299	0.534
$\Delta E_{Q,1}$ (mm s^{-1})			1.619	1.345
σ_1 (mm s^{-1})			0.910	0.821
p_1 (mm s^{-1})			0.125	0.173
γ (mm s^{-1})	0.431	0.267	0.228	0.250
δ_0 (mm s^{-1})	0.487	0.474	0.472	0.457
δ_1 (mm s^{-1})	−0.042	−0.028	−0.025	−0.022
h_1/h_{-1}	0.963	0.955	0.954	1.005
δ (mm s^{-1})				-0.511
ΔE_Q (mm s^{-1})				0.262
γ (mm s^{-1})				0.250
Area				0.024
Red. χ^2	1.740	0.682	0.615	0.567

As expected for a nanoparticle structure, the line shapes are not Lorentzian, but rather Voigt[27]. The Fe(III) signal was modeled using a distribution of hyperfine parameters. To fully capture the observed shoulder, it was necessary to include a separate component in the simulation with $\delta = -0.51$ and $\Delta E_Q = 0.26$ mm s^{-1}. The low isomer shift of this component is consistent with the presence of a small amount (~ 2.5%) of Fe in an oxidation state greater than Fe(III). This isomer shift is also significantly more negative than that previously assigned to Fe(IV) in [NiFe]-LDH by *in-situ* Mössbauer (−0.27 mm s^{-1})[3].

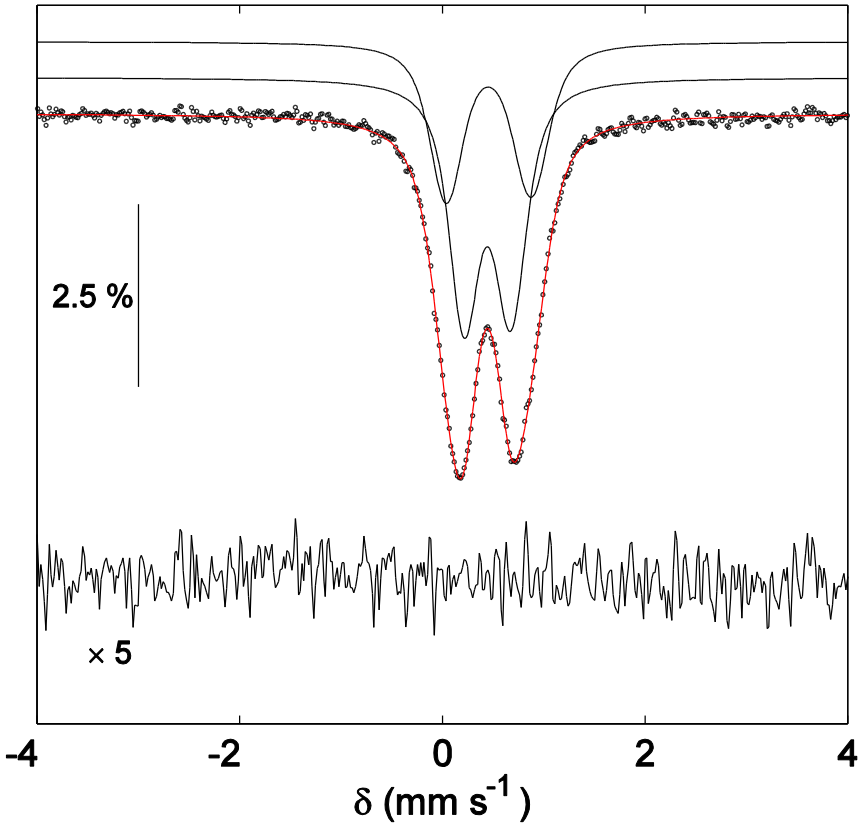

Figure S21: The zero field Mössbauer spectrum of [Ni^{57}Fe]-LDH, polarized at 1 V *vs.* Pt, collected at 100 K. The raw data are presented as open black circles, with the simulated spectrum shown in red. Individual sub-spectra are plotted as black lines above the raw data. Below is shown a subtraction of the simulated Fe(III) components from the data.

Table S4: Simulation for [Ni^{57}Fe]-LDH, polarized at 1 V *vs.* Pt, at 100 K using a hyperfine distribution model.

	Parameters	
	***N* = 1**	***N* = 2 (Final)**
$\Delta E_{Q,1}$ (mm s^{-1})	0.606	0.470
σ_1 (mm s^{-1})	0.559	0.350
p_1 (mm s^{-1})	0.997	0.608
$\Delta E_{Q,1}$ (mm s^{-1})		0.853
σ_1 (mm s^{-1})		0.430
p_1 (mm s^{-1})		0.384
$\Delta E_{Q,1}$ (mm s^{-1})		
σ_1 (mm s^{-1})		
p_1 (mm s^{-1})		
γ (mm s^{-1})	0.297	0.277
δ_0 (mm s^{-1})	0.423	0.430
δ_1 (mm s^{-1})	0.041	0.030
h_1/h_{-1}	1.015	1.005
Red. χ^2	0.910	0.591

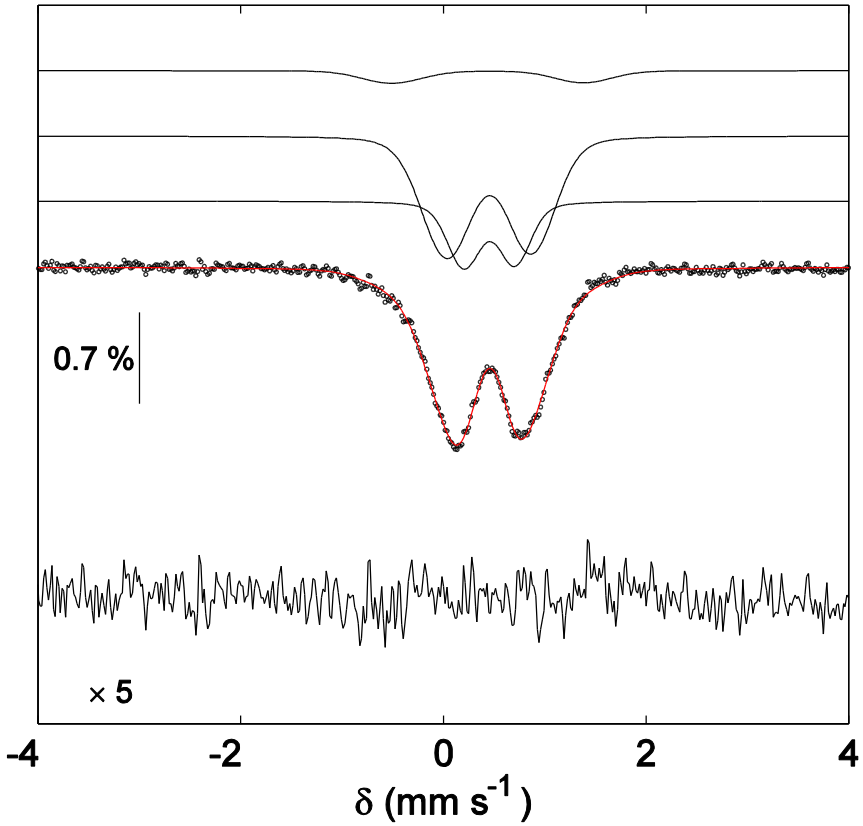

Figure S22: The zero field Mössbauer spectrum of [Ni^{57}Fe]-LDH, initially polarized at 2 V *vs.* Pt and then quenched in 1% 1 M aqueous KOH in acetonitrile, collected at 100 K. The raw data are presented as open black circles, with the simulated spectrum shown in red. Individual sub-spectra are plotted as black lines above the raw data. Below is shown a subtraction of the simulated Fe(III) components from the data.

Table S5: Simulation for [Ni^{57}Fe]-LDH, after quenching, at 100 K using a hyperfine distribution model.

	Parameters		
	***N* = 1**	***N* = 2**	***N* = 3 (Final)**
$\Delta E_{Q,1}$ (mm s^{-1})	0.737	0.606	0.503
σ_1 (mm s^{-1})	0.568	0.616	0.610
p_1 (mm s^{-1})	1.044	0.497	0.243
$\Delta E_{Q,1}$ (mm s^{-1})		0.977	0.834
σ_1 (mm s^{-1})		1.116	1.011
p_1 (mm s^{-1})		0.485	0.650
$\Delta E_{Q,1}$ (mm s^{-1})			1.888
σ_1 (mm s^{-1})			1.228
p_1 (mm s^{-1})			0.081
γ (mm s^{-1})	0.423	0.224	0.133
δ_0 (mm s^{-1})	0.462	0.465	0.460
δ_1 (mm s^{-1})	−0.015	−0.020	−0.013
h_1/h_{-1}	0.930	0.915	0.922
Red. χ^2	0.854	0.608	0.562

S9: Mössbauer DFT Calculations

We performed DFT calculations on (1) single-site iron(VI) with three hydroxides and two oxos in which all atoms could be optimized; the apparent δ was calculated to be –0.68 mm s^{-1}. When (2) the hydroxides were constrained to the lattice geometry, the isomer shift of Fe(VI) was calculated to be more positive, at –0.20 mm s^{-1}. A third calculation involving (3) a 3-atom cluster of one Fe(VI) and two Al atoms yielded δ = −0.24 mm s^{-1}. The computationally predicted limits for the isomer shift of iron(VI) in this environment, −0.20 > δ > −0.68 mm s^{-1} bound the experimentally observed isomer shift.

Table S6: Optimized XYZ Coordinates for Structure (1)

Fe	-0.690080	0.296960	0.083917
O	-1.520038	0.233082	-1.287683
O	-1.577314	0.102829	1.386443
O	-0.636183	2.180651	0.155390
H	0.306126	2.335936	0.292712
O	1.104634	0.417935	0.208686
H	1.306126	-0.527962	0.089503
O	-0.222987	-1.607816	-0.071702
H	-0.703344	-1.889603	-0.857256

Table S7: Optimized XYZ Coordinates for Structure (2)

O	-10.749130	-14.834910	-85.247750
H	-10.598380	-14.951450	-84.418550
O	-9.792532	-14.730370	-87.564745
O	-7.745810	-14.879370	-85.800020
H	-7.595060	-14.995910	-84.970820
Fe	-9.280415	-13.942997	-86.235214
O	-9.144440	-12.237510	-85.174450
H	-8.993680	-12.354050	-84.345250
O	-8.465366	-12.728183	-87.283347

Table S8: Optimized XYZ Coordinates for Structure (3)

O	-8.788652	-17.643786	-85.403046
H	-9.777944	-17.596749	-85.452083
Al	-8.020719	-16.754324	-86.826464
O	-8.882086	-17.501167	-88.358745
O	-6.480453	-17.960877	-86.746751
H	-8.845428	-16.861806	-89.120542
H	-6.424330	-18.455793	-85.891083
O	-9.424174	-15.507026	-87.153450
O	-7.015195	-15.395179	-85.867215
H	-8.985117	-14.523138	-87.460767
H	-7.150883	-15.183164	-84.918024
Fe	-5.055821	-16.689395	-87.010543
O	-4.369233	-17.237178	-88.412184
O	-4.192848	-17.123038	-85.670835
Al	-6.373639	-13.995212	-87.154537
O	-6.643808	-15.812771	-88.058299
O	-4.565959	-14.818499	-86.941442
H	-6.454896	-15.890825	-89.022355
H	-4.188726	-14.603993	-86.048707
O	-8.177826	-13.411545	-87.518373
O	-5.964849	-12.788684	-85.800180
H	-8.101977	-12.946162	-88.394605
H	-6.737206	-12.172836	-85.689154
O	-5.905367	-13.205499	-88.788502
H	-4.918306	-13.145434	-88.866183